Ultramicroscopy 253 (2023) 113818

Contents lists available at ScienceDirect

Ultramicroscopy

journal homepage: www.elsevier.com/locate/ultramic

Four-dimensional electron energy-loss spectroscopy

Mei Wu [a,b], Ruochen Shi [a,b], Ruishi Qi [c], Yuehui Li [a,b], Jinlong Du [b], Peng Gao [a,b,d,e,*]

[a] International Center for Quantum Materials, Peking University, Beijing 100871, China
[b] Electron Microscopy Laboratory, School of Physics, Peking University, Beijing 100871, China
[c] Department of Physics, University of California at Berkeley, Berkeley 94720, United States
[d] Collaborative Innovation Center of Quantum Matter, Beijing 100871, China
[e] Interdisciplinary Institute of Light-Element Quantum Materials and Research Center for Light-Element Advanced Materials, Peking University, Beijing 100871, China

ARTICLE INFO

Keywords:
Scanning transmission electron microscopy (STEM)
Four-dimensional electron energy-loss spectroscopy (4D-EELS)
Phonon dispersion
Defect scattering

ABSTRACT

Recent advances in scanning transmission electron microscopy have enabled atomic-scale focused, coherent, and monochromatic electron probes, achieving nanoscale spatial resolution, meV energy resolution, sufficient momentum resolution, and a wide energy detection range in electron energy-loss spectroscopy (EELS). A four-dimensional EELS (4D-EELS) dataset can be recorded with a slot aperture selecting the specific momentum direction in the diffraction plane and the beam scanning in two spatial dimensions. In this paper, the basic principle of the 4D-EELS technique and a few examples of its application are presented. In addition to parallelly acquired dispersion with energy down to a lattice vibration scale, it can map the real space variation of any EELS spectrum features with a specific momentum transfer and energy loss to study various locally inhomogeneous scattering processes. Furthermore, simple mathematical combinations associating the spectra at different momenta are feasible from the 4D dataset, e.g., the efficient acquisition of a reliable electron magnetic circular dichroism (EMCD) signal is demonstrated. This 4D-EELS technique provides new opportunities to probe the local dispersion and related physical properties at the nanoscale.

1. Introduction

The dispersion relation of elementary excitations is fundamental in solid physics, describing elementary quasiparticles and their couplings in condensed matter systems. For example, the electron band structure determines the transport behavior of a solid, correlates with photoelectric excitations, such as indirect/direct interband transitions [1–4] and excitons [5], and serves as a crucial signature of different ordered states [6–8]. It is also related to the electromagnetic behavior in superconductors, determining the superfluid weight [9] and Fermi velocity [10]. For lattice vibrations, the phonon dispersion offers absorption/emission at infrared/THz frequencies [11–17]. Phonons are primary heat carriers in most nonmetallic solids. Therefore, the phonon dispersion is crucial for determining the thermal properties of materials [18–23], i.e., the thermal conductivity of a material is closely related to the differential of dispersion (determines the phonon group velocity), the line width of dispersion (determines the phonon lifetime), and phonon density of states (derived from the dispersion relation and determines the heat capacity) [22]. For electron–phonon coupling that is critical in electrical transport properties, the interaction strength depends on the momentum transfer in the dispersion [24]. The softening of the phonon modes driving the phase transition might occur at specific positions in the Brillouin zone, requiring the dispersion of knowledge.

Since the momentum of a phonon (**q**) implies a spatial frequency, the variation of spatial translational symmetry alters the energy dispersion. The structural dimensions of materials and devices are rapidly approaching the nanometer length scale. The reduced size can cause many emergent phenomena unavailable in bulk materials [25–32]. Such nanotechnology has shown broad applications in electronics [33], energy [34], the environment [35], and biomedicine [36]. Taking a phonon as an example, at the interface, surface, and structural defects with discontinued chemical bonds, local phonon modes typically emerge [24,37–40]. The phonon modes for nanostructures with huge specific surface areas should differ from the bulk states. Typically, these local phonon modes, described by local phonon dispersion, will significantly affect the physical properties in the low dimensional systems. For example, nanoscale inhomogeneities can enhance phonon scattering and suppress thermal conductivity [41–44], which delivers essential information for defect engineering in thermal management materials. The interface phonon modes in heterostructures with two-dimensional

* Corresponding author at: International Center for Quantum Materials, Peking University, Beijing 100871, China.
E-mail address: p-gao@pku.edu.cn (P. Gao).

https://doi.org/10.1016/j.ultramic.2023.113818
Received 19 January 2023; Received in revised form 20 June 2023; Accepted 25 July 2023
Available online 28 July 2023

electron gas or interface/surface superconductivity are critical for electrical transport properties [45]. Due to the confinement effects, the energy and the symmetry of the surface phonon polariton modes also depend on the size of the nanostructures [46–48]. Hence, it is crucial to unveil the nanoscale dispersion to directly correlate the energy (E), $\mathbf{q}$, and space (x) variations.

Such a local dispersion measurement requires a technique to achieve high energy, momentum, and spatial resolutions simultaneously. Fig. 1 summarizes the resolutions in advanced characterization techniques to study the nanoscale dispersion. Inelastic neutron/X-ray scatterings (INS/IXS) are powerful in studying the phonon dispersion of bulk crystals [49], but high-spatial resolution is lacking due to their large beam size. The demand for large-scale experimental setups and large-size single-crystal specimens also limits their use. Optical methods, such as tip-enhanced Raman scattering and infrared absorption based on scanning near-field optical microscopes (SNOM), can attain high energy and decent spatial resolutions [37,50–52]. However, restricted by the inherent property of an optical probe, optical methods primarily provide information about essentially zero-momentum transfer [53]. High-resolution electron energy-loss spectroscopy (EELS) (HREELS) is used to detect lattice vibrations but is only sensitive to surface signals. Due to the low acceleration voltage in HREELS, the corresponding spatial resolution is poor [54]. Recently, advances in EELS in scanning transmission electron microscopy (STEM) [55,56] have made it possible to form the atomic-scale focused, coherent, and monochromatic electron probe [57–60]. Due to the picometer-level de Broglie wavelengths of high-energy electrons, electron microscopy naturally realizes high-spatial resolution and detection sensitivity, ideal for studying the nanostructure [61–65]. The small wavelength of electrons indicates a large momentum exchange range. The attainable coherent and monochromatic electron beam with high brightness further delivers milli-electronvolt energy resolution and a sufficient momentum detection range and resolution [38,56–58,66–72]. Particularly, the recently developed four-dimensional EELS (4D-EELS) technique, containing four-dimensional information about the energy, momentum, and two spatial dimensions, is powerful to probe the dispersion at the nanometer scale [24,73–75].

Here, we summarize some applications of the 4D-EELS technique in investigating nanoscale dispersion and beyond. By placing a slot aperture in the diffraction plane to select a specific momentum transfer direction, the dispersion diagram can be parallelly acquired within a short acquisition time. During sample scanning, the recorded 4D dataset is a matrix of E–$\mathbf{q}$ maps as the function of the scanning position in real space. Due to the breakthrough of energy resolution in STEM-EELS with a cold gun and monochromator, this technique could recently detect momentum-dependent lattice vibrations. Moreover, stacks of momentum-resolved energy-filtered images extracted from the 4D dataset can visualize and distinguish local inhomogeneity at the nanoscale. We can also subtract or integrate the electron energy-loss (EEL) spectra at different reciprocal locations, elucidating momentum-related physical properties and dynamical processes, such as obtaining a reliable, high-efficiency electron magnetic circular dichroism (EMCD) signal. The flexibility of the experimental setup and the extractability of multidimensional information in nanostructures provide new opportunities to probe the thermal, electrical, optical, and mechanical properties in interface science and nanoscience. In the following, we introduce the available multidimensional information and the corresponding resolution in electron microscopy. Next, we discuss the applications of 4D-EELS in probing phonon dispersion and then extend to some electronic excitation.

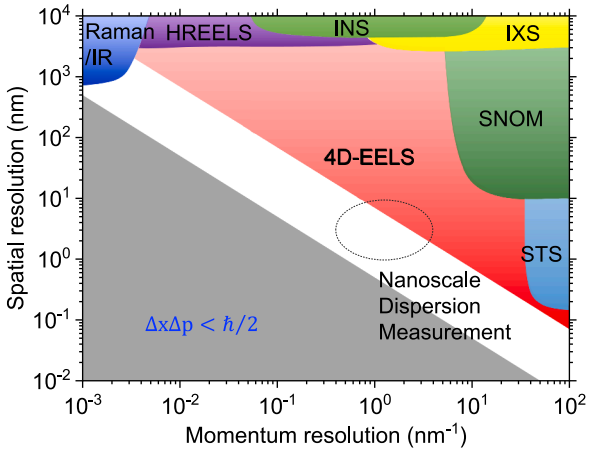

Fig. 1. The spatial and momentum resolving power of different techniques. Scanning near-field optical microscopy (SNOM). Infrared (IR) absorption spectroscopy. Inelastic neutron/X-ray scatterings (INS/IXS). High-resolution electron energy-loss spectroscopy (HREELS).

2. Experimental

2.1. Multidimensional information in electron microscopy

Fig. 2a shows the fundamental transmission electron microscopy geometry. Kiloelectronvolt electrons pass through the magnetic lens and are focused onto the sample, propagating through and scatter with the sample, resulting in the elastically and inelastically scattered electrons in postspecimen electron optics containing abundant information. The capability of measuring nanoscale dispersion in electron microscopy is achieved by setting different detectors at different crossover positions in the electron optics to select and analyze the scattered electrons. Specifically, the structural information can routinely be extracted from the high-angle annular dark-field (HAADF) detector. The scattered electrons will form a diffraction pattern at the back focal/diffraction plane, representing the reciprocal/momentum space of the specimen. Manipulating the postspecimen electron optics allows the switching between real and momentum space. Moreover, the entrance aperture in the diffraction plane can select the scattered electrons with a specific momentum range, which further pass through the projector lens and EELS spectrometer and are finally collected by the EELS detector. It can detect a wide energy range and implies multiple physical processes [55,76]. The typical acquired EELS signal comprises a zero-loss peak (ZLP) corresponding to the elastic scattering and an energy loss part signifying inelastic scattering information with specific momentum ($\hbar\mathbf{q}$) and energy transfer ($\hbar\omega$). In principle, we can obtain the specimen properties of the spatial, momentum, and energy dimensions by recording the above signals in different detectors.

In detail, as presented in Fig. 2b, by combining a real space scan and the momentum information in the diffraction pattern, different STEM images, such as bright field, dark-field [77,78], and 4D-STEM images [79,80], are extracted, mapping the underlying nanostructure, atomic-scale electric field, and charge distribution. In addition to the imaging characterization, adjusting the projector lenses to rotate and scale the scattered beam allows us to select a specific momentum direction to enter the EELS spectrometer, obtaining the momentum-resolved EELS and identifying different dispersion branches [58,67,81]. A three-dimensional dataset comprising the EELS spectra and the corresponding two-dimensional scanning position of the specimen will correlate bonding, chemical, and structure information [76, 82]. The above measurements have been the mature and standard analysis methods in STEM, but all lack the information in a specific dimension. The recently developed 4D-EELS technique records the two-dimensional region in real space and the two-dimensional intensity map versus energy and momentum transfer associated with each scanning point [24,73], simultaneously encompassing spatial, momentum, and energy information.

Fig. 3a shows the multidimensional information recorded by 4D-ELLS. This 4D hyperspectral data cube is a collection of a series of

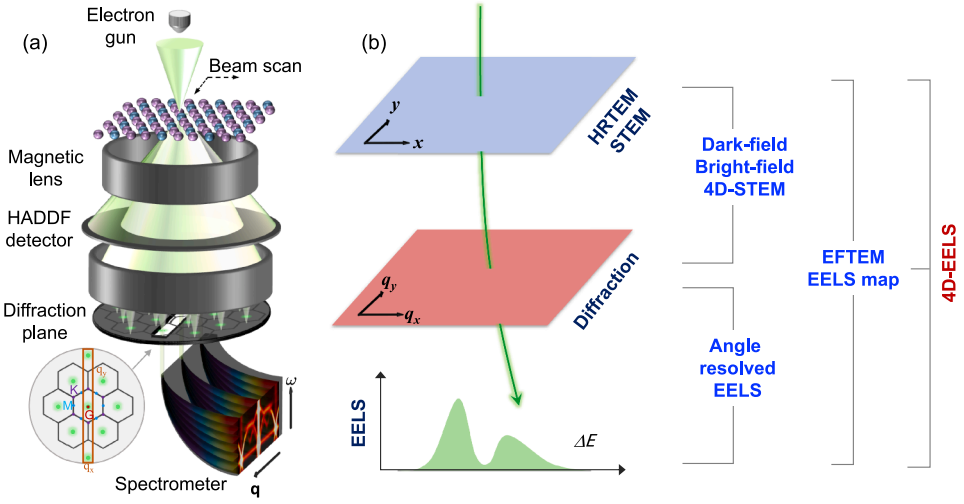

Fig. 2. Schematics of the experimental setup and obtained information in 4D-EELS. (a) Illustration of the beam geometry in 4D-EELS measurement. The reciprocal space of h-BN with high-symmetry points is also inset as a typical example. (b) Different operating modes in transmission electron microscopy (TEM) using single or combinations among spatial, momentum, and energy information.

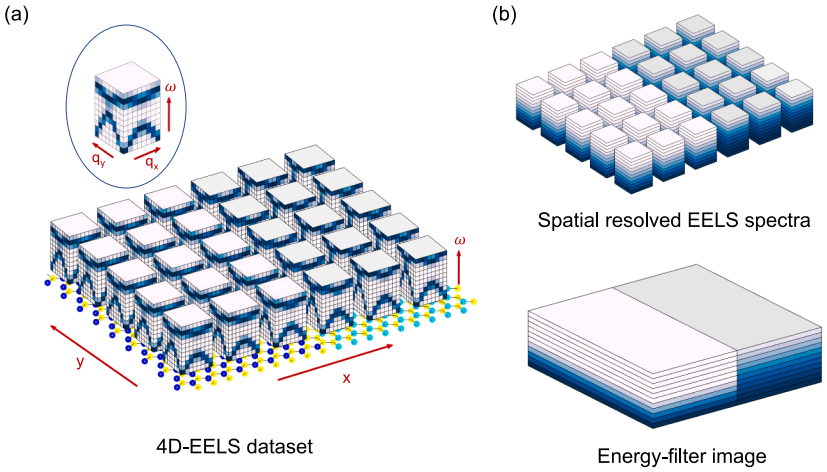

Fig. 3. Schematic diagram of available multidimensional information in 4D-EELS. (a) The assembly of the 4D data tube. The individual bit contains the E–$\mathbf{q}$ maps recorded on a pixel (dx, dy) in real space ($\boldsymbol{x}$, $\boldsymbol{y}$). (b) The schematics of the extracted spatial-resolved EELS spectra (top panel) and energy-filtered image (bottom panel) from the 4d dataset.

momentum-resolved EELS maps (E, $\mathbf{q}$) (the lateral face in the cube) and the corresponding region of interest in the sample (the top face in the cube), correlating the spatial and dispersion diagram. The individual cube represents the fundamental component in the 4D dataset, containing the scan location of a single pixel in real space and corresponding recorded E–$\mathbf{q}$ maps. In the experiment, the pixelated E–$\mathbf{q}$ map is obtained by properly placing a slot aperture oriented normal to the spectrometer dispersion ($\boldsymbol{q_y}$ direction, the slot aperture orientation, and the momentum transfer direction), typically parallel to a high-symmetry line in Brillion zones (BZs). The $\boldsymbol{q_x}$ dimension in the slot aperture is integrated, and the acquired data displays the $\boldsymbol{q_y}$ and E dependence. Previous studies have attempted to measure the momentum-resolved EELS maps by beam deflection or serially moving the collection aperture relative to the diffraction plane to ensure the EELS spectra along a specific momentum direction can be collected in the spectrometer entrance [58,67]. However, the typical acquisition time for these approaches is from tens of minutes to several hours [58,67] for one space point. Placing the slot aperture at the diffraction plane [81,83] is more efficient to parallelly map high signal–noise ratio (SNR) phonon dispersion within a shorter acquisition time (a few seconds). This setup is also advantageous for data consistency among different momentum points. Combined with the scanning illumination recording the structural information ($\boldsymbol{x}$, $\boldsymbol{y}$) using a HAADF detector, the ($\boldsymbol{x}$, $\boldsymbol{y}$, E, $\boldsymbol{q}$) 4D dataset is formed. We can also selectively omit one or two dimensions from this dataset to obtain the above three-dimensional or two-dimensional datasets. For example, as shown in Fig. 3b, we can extract the spatial-resolved energy-loss map or select a specific energy to obtain a series of energy-filtered images.

Furthermore, the advance in electron microscopy equipment over the past decades has broadened the research field of electron microscopy studies. The spherical aberration corrector promotes spatial resolution [84]. The progress in the monochromator and spectrometers with multipole correctors produces a narrow and small-tailed ZLP and improves the energy resolution [57,60,66,85], previously limited by the spread of the electrons from the gun. The attainable EELS details are down to THz frequencies, enabling studying some low-loss excitation, such as exciton [86], plasmon [87], and phonon dispersions [24,38,70,73,88–90]. The minimalized ZLP tail decreases the spectra background and ensures the precise extraction of the signal of interest. Besides, the progress in detectors with a high dynamic range and good quantum

detection efficiency improves the acquired data reliability and accuracy [91]. The widespread availability of computational power and simulations contributes to the data analysis and quick extraction of the required information.

2.2. The accessibility and constraint of different resolutions

Fundamentally, the size of the corresponding crossover (i.e., the demagnified image of the electron source, also known as the probe) determines the spatial, momentum, and energy resolutions in the electron optics [66,71]. After minimizing the instrument instabilities well enough, ideally, the diffraction limit becomes the fundamental limit. The size of the crossover is expressed as [24,59,66,92]

$$d_m = \left\{ \left[\frac{2}{\pi} \left(\frac{I_P}{B} \right)^{0.5} \frac{1}{\alpha} \right]^2 + \left(1.22 \frac{\lambda}{\alpha} \right)^2 \right\}^{0.5},$$

where λ denotes the electron wavelength, α is the semi-angle of the electron beam converging on the crossover, I_P represents the probe current, and B is the source brightness. Hence, the spatial resolution (the probe size at the sample) is inversely proportional to the corresponding convergence semi-angle (α) and the primary energy (E_0). The beam size as a function of α at primary energies of 30 kV, 60 kV, and 100 kV is plotted in Fig. 4a.

The uncertainty principle limits the momentum resolution, indicating the intrinsic tradeoff between spatial and momentum resolution. Fig. 4b shows the relation between the convergence semi-angle at the sample and the diffraction spots radius. The BZ size of a diamond is marked as the reference. A 10 mrad convergence semi-angle at 60 kV is approximately equivalent to the BZ size of the diamond, and the larger convergence angle will lead to the overlap among neighboring BZs, mixing scattering signals with momenta along all directions. Therefore, the momentum-resolved energy-loss spectroscopy must use a nanometer-sized electron probe with a small convergence semi-angle to ensure enough momentum resolution (typically at least one-quarter of the BZ lateral size) [24]. Fig. 4c shows the acquired E–$\mathbf{q}$ maps with different convergence semi-angles at the 30 kV and 60 kV primary energy. As the convergence semi-angle increases, the central diffraction spot increases, and the dispersion becomes blurred.

The crossovers and the energy dispersion at the monochromator slit and the EELS detector determine the energy resolution, where the aberration correction in the slit and the spectrometer will improve the energy resolution [59,66]. However, the minimum usable post-slit beam current for spectroscopy requires a specific probe current at the silt, unavoidably worsening the attainable energy resolution [59]. Based on these limitations, the energy resolution at 60 kV can attain 3.2 meV in this experiment [93]. Besides, the energy resolution is proportional to the square root of the primary energy [60,66]. As shown in Fig. 4c, the phonon dispersion measured at 30 kV shows sharper and more detailed features than at 60 kV.

Hence, it requires balancing the spatial, momentum, and energy resolutions based on the different experimental purposes. In practice, we need a reasonable compromise for the resolution and the corresponding SNR. First, to obtain a high SNR, the acquisition time can be increased at the expense of energy and spatial resolutions due to possible drifts. Second, the wider energy-selecting slit will increase the probe current to acquire the weak signal where the intensity of the energy loss is 10^2–10^4 times less than the ZLP but might worsen the energy resolution. A large dispersion (low eV/channel) will minimize the full width at half maxima (FWHM) of the ZLP but could decrease the SNR. We must choose different settings based on the signal with varying energy ranges and spectra features. Due to the multidimensional and complex information in the 4D-EELS technique, data analysis is critical. The data processing, such as beam energy drift-correcting, noise removal, and deconvolution by the angle distribution of the incident beam [24,83], is beneficial for extracting accurate signals. The following two sections discuss the 4D-EELS measurements and related physical processes in phonon modes.

2.3. Experimental setup of 4D-EELS

The 4D-EELS were recorded using a Nion HERMES 200 microscope operating at 60 kV and 30 kV. By optically rotating the postspecimen beam to a fixed slot aperture, we can select a specific diffraction pattern

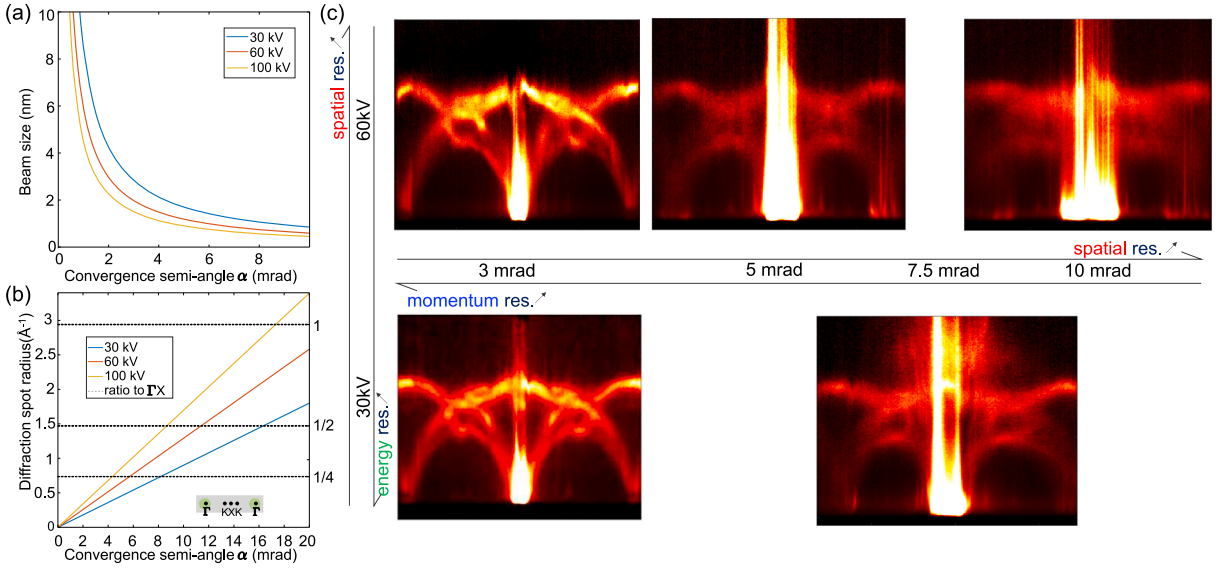

Fig. 4. The tradeoff relation between the spatial, momentum, and energy resolution as a function of the convergence semi-angle and primary energy. (a, b) Spatial resolution (a) and momentum resolution (b) vary with convergence semi-angles at 100 kV (orange), 60 kV (red), and 30 kV (blue) primary beam energy. A larger convergence semi-angle can attain a higher spatial resolution. The momentum resolution depends on the convergence and collection semi-angles. For example, the dashed horizontal lines in (b) represent the ratio of the Γ–X distance of the diamond. The corresponding typical configuration of the diffraction spot (green circles) and the slot aperture (gray rectangle) in the 4D-EELS measurement is also inserted. (c) The beam energy and convergence semi-angle dependence of the measured diamond phonon dispersion. The collection angle of the slot aperture was 4.5 × 75 mrad. As the convergence semi-angle increases, the central diffraction spot increases, and the dispersion becomes blurred. For the primary energy, the dispersion measured at 30 kV shows sharper and more detailed profiles than at 60 kV.

entering the EELS entrance with desired orientation and obtain the corresponding *E*–***q*** diagram. The uncertainty principle precludes the possibility of obtaining best spatial and momentum resolutions simultaneously. Thus, to ensure enough momentum resolution for the measurement of decent dispersion curve, the electron probe we usually utilized is 1.5 mrad convergence semi-angle at 60 kV, which corresponds to approximately spatial resolution of ~4 nm.

The typical dwell time for recording 4D-EELS datasets was 15 s/pixel. The dispersion was a 0.0005 eV/channel with typical energy resolution (FWHM of the elastic line) 14–16 meV. The corresponding momentum range was $0 < q < 10$ Å^{-1}, and the momentum resolution was ~0.2 Å^{-1}, which can be estimated by the convergence semi-angle and geometry of the slot aperture.

All acquired spectra were processed by custom-written MATLAB code [24]. The EELS spectra were registered by their normalized cross-correlation for each dataset to correct beam energy drifts. The 4D-EELS datasets were individually denoised in two spatial dimensions for each energy and momentum channel. The noise level was estimated based on the high-frequency elements in the Fourier domain. A correction for the statistical factor was conducted following the literature [94] to reduce the influence of elastic peak.

2.4. Phonon dispersion in 4D-EELS

The recent breakthrough in energy resolution in STEM-EELS promotes researching the 4D-EELS technique in probing phonons, the quantized modes of lattice vibration. Fig. 5 shows the typical phonon dispersion diagram acquired by the 4D-EELS technique. The vertical axis corresponds to the energy loss, and the horizontal axis represents the momentum q_y. As shown in Fig. 5b, the bright spot corresponds to the diffraction spot in the diffraction plane, where the central diffraction spot refers to zero-momentum transfer. The colored intensity in the diagram is determined by the double differential cross-section, providing the probability of detecting scattered electrons in a scattering angle element $d\Omega$ with an energy loss ($d\omega$) compared to its initial energy E_0 expressed as [24,58,73,95–98]

$$\frac{\mathrm{d}^2\sigma}{\mathrm{d}\omega \mathrm{d}\Omega} \propto \sum_{mode\ \lambda} |\mathrm{F}_\lambda(\mathbf{q})|^2 \left[\frac{n_\mathrm{q}+1}{\omega_\lambda(\mathbf{q})}\delta(\omega-\omega_\lambda(\mathbf{q})) + \frac{n_\mathrm{q}}{\omega_\lambda(\mathbf{q})}\delta(\omega+\omega_\lambda(\mathbf{q}))\right],$$

where **q** denotes the momentum transfer and equals a reciprocal lattice vector of material, λ labels the phonon branch, $\omega_\lambda(\mathbf{q})$ is the momentum-dependent phonon frequency, n_q is the occupation number, $\mathrm{F}_\lambda(\mathbf{q})$ is a fundamental parameter describing the coupling strength for fast electron scattering involving the vibrational mode, and $\delta(\mathrm{x})$ is the Dirac delta function. After correction for the statistical factor, the acquired *E*–**q** diagram is proportional to $\sum_{mode\ \lambda} |\mathrm{F}_\lambda(\mathbf{q})|^2$, where

$$\mathrm{F}_\lambda(\mathbf{q}) \propto \frac{1}{q^2}\sum_{atom\ k}\frac{1}{\sqrt{M_k}} e^{-\mathrm{i}\mathbf{q}\cdot\mathbf{r}_k} e^{-W_k(\mathbf{q})}\ Z_k(\mathbf{q})\ [\mathbf{e}_\lambda(k,\mathbf{q})\cdot\mathbf{q}].$$

k labels the atom in the unit cell. M_k, Z_k (**q**), and $\mathbf{r}_k$ are the mass, the effective charge, and the real space position vectors of the kth ion, respectively. The effective charge $Z_k(\mathbf{q})$ is calculated using atomic form factors [96,99]. $\mathbf{e}_\lambda(k,\mathbf{q})$ represents the phonon displacement eigenvectors.

Based on the above expression of the scattering cross-section, we can understand the relative contributions of the different modes to the *E*–**q** map. First, the q-dependent scattering cross-sections result in the asymmetric acquire EELS at different momentum transfers. Second, the dot product of the electron momentum transfer **q** and the displacement vector of the kth atom and λth mode $\mathbf{e}_\lambda(k,\mathbf{q})$ implies that those modes with nonzero vibration displacement along the **q** direction predominately contribute to the *E*-**q** map intensity. Hence, when we place the slot at the position of the blue rectangle in Fig. 5a, the displacement vector $\mathbf{q}_1$ of transverse modes such as TO and TA modes perpendicular to **q** and these modes will be inactive in EELS shown in Fig. 5b. However, if we displace the slot aperture to the green position in Fig. 5a, these modes will become active as shown in Fig. 5c. This is because the electron momentum now is along the $\mathbf{q}_2$ direction and therefore **q** dots **e** will no longer be zero for transverse modes.

However, the different scattering processes dominate the obtained signal at different momentum transfers. Factor $1/\mathrm{q}^2$ highly modifies the recorded signal at the small momentum transfer [97], resulting in strong intensity for Bragg spots, affecting the signal quality of low-energy acoustic phonon modes. The dipole scattering with the delocalization nature is proportional to $1/\mathrm{q}^2$, thus having a large scattering cross-section in the long wavelength limit (momentum $q = 0$ Å^{-1}) [100]. At the large q, the localized impact scattering will mostly contribute to the spectra [61,101,102]. The conventional acquired EELS signals lack momentum resolution and typically mix the two phonon scattering processes. The typical way to collect scattered electrons with different momentum transfers is by deflecting the beam after or before the sample [65,100]. The 4D-EELS technique can simultaneously record the signal at different momentum transfers and flexibly extract the nanoscale real space distribution of different phonon modes with specific momentum transfer. Specifically, by extracting the signal in the long wavelength limit, we can probe some low-loss nanophotonic excitations in the mid-infrared to terahertz ranges with a high Q factor, showing promising applications in nano optics [75,103,104]. We can map different phonon modes after excluding the signal at a small q. We can also integrate the signals containing more than one BZ of momentum space, and the obtained spectra will preferably be closer to phonon DOS. The following section will explain a more detailed application of the 4D-EELS technique.

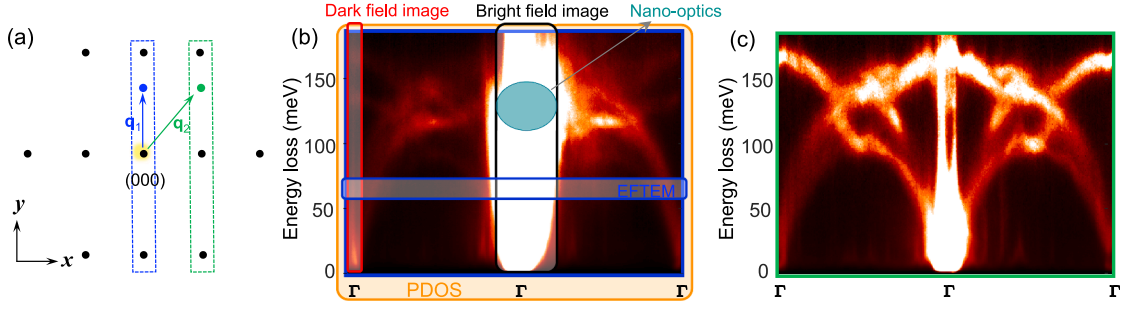

Fig. 5. Comparison of the obtained E–q maps at different momentum transfers. (a) Schematic of geometry showing the position of the slot aperture in the first Brillion Zone (BZ) (blue rectangle) and higher-order BZ (green rectangle). (b, c) The corresponding acquired E–q maps when the slot aperture places at the position of blue and green rectangle in (a), respectively. More phonon branches are visible in the maps of higher-order BZs. The typical phonon dispersion recorded by the 4D-ELLS and the corresponding extractable information by choosing suitable energy and momentum windows are also illustrated in (a).

3. Results

3.1. Energy and momentum filtered in 4D-EELS

3.1.1. Elemental sensitive mapping

We introduce new 4D-EELS applications for nanoscale real space mapping with specific momentum transfer and energy loss. We chose the cubic boron nitride (cBN)/diamond heterointerface as the model system. The atomically resolved HAADF image in Fig. 6a shows the atomically sharp and coherent interface. Fig. 6b shows that the bulk cBN and diamond have similar phonon dispersion profiles with a large degree of overlap of phonon DOS. However, that cBN features an obvious longitudinal optical–transverse optical splitting gap at the Γ point. Fig. 6c and d shows the phonon dispersion curves along Γ–K–X–K–Γ measured at the diamond and cBN sides, respectively, correlating well with the calculated phonon dispersion. A convergence semi-angle of 1.5 mrad was used to ensure enough momentum resolution. A reciprocal lattice vector displaces the slot aperture along the Γ–K–X–K–Γ line to avoid the strong central diffraction spot and activate more phonon modes. The beam geometry is similar to the position of the green rectangle in Fig. 5. Previous energy-filtered (EF) TEM imaging techniques are typically equipped with specific energy filter attachments [105–107]. One specific energy is selected, and the energy-filtered image containing the corresponding spatial distribution of spectral intensity is formed. This setup makes the selected energy of the EELS spectrum integrate over a large range of **q** vectors. The 4D-EELS technique provides convenience to extract the same information by selecting an area with specific energy loss and momentum transfer in the recorded dispersion mapping of the 4D dataset during data processing. Then, we can obtain the corresponding real space image of the selected range using the information with the momentum and energy dimensions simultaneously.

For example, as marked by the purple rectangle in Fig. 6b, the phonon DOS has a large overlap from 80 meV to 100 meV. Hence, if we only select the electrons with an energy loss from 80 meV to 100 meV, the corresponding image has uniform intensity profiles (Fig. 6e). However, from the corresponding *E*–**q** maps in the 4D-EELS dataset, we can separate the cBN and diamond at specific momentum transfer and obtain elementally sensitive images. In Fig. 6f, when selecting the red rectangle range in the *E*–**q** maps, the high intensity primarily occurs at the diamond side, showing an abrupt intensity change at the interface. The spatial distribution of the blue rectangle range is also shown in Fig. 6g, where a very strong intensity in cBN is visible. More particular stacks of energy and momentum-filtered images can be extracted via the 4D-EELS technique.

3.1.2. Different defects mapping and diffraction contrast decoupling

Due to the ability to form the image in the real space of any spectral feature, the 4D-EELS can provide a chance to decouple the scattering contributions in the traditional bright and dark-field images. Fig. 7a shows the HAADF image of multiwalled boron nitride nanotubes (BNNTs), where multiple voids or defects and resulting defect scatterings (elastic and inelastic) exist inside this structure. Due to the strong dynamical effect in electron diffractions, the dark-field image is sensitive to crystal defects and is a powerful imaging mode for defects. The 4D-EELS technique can further identify the energy loss with different scattering processes at varying momentum transfers. Here we spatially map the different energy ranges of the EEL spectra in the central diffraction and second-order diffraction spots, separately shown in Fig. 7b–g.

First, Fig. 7b and e show that the different momentum transfers result in different intensity profiles. The real space map of the overall EELS spectrum extracted from the central diffraction spot and the secondary diffraction spot are fundamentally consistent with the bright field and

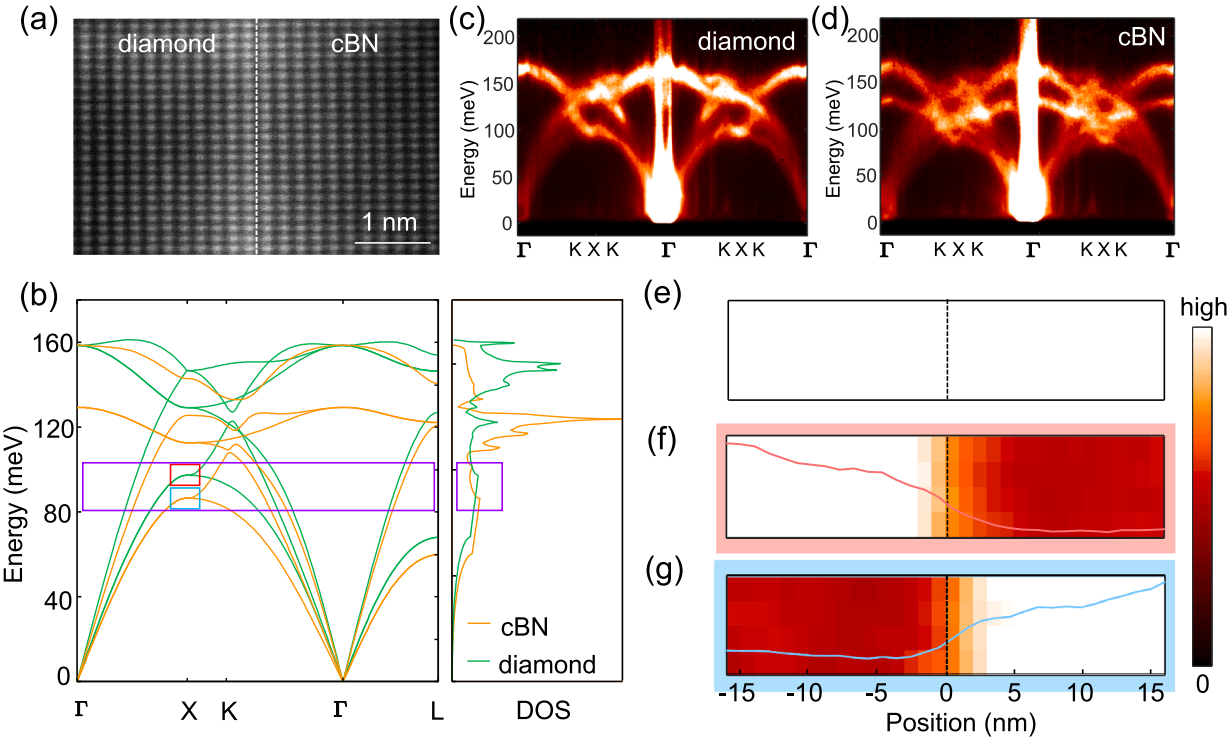

Fig. 6. Energy-filtered image at a specific momentum. (a) The HAADF image of the diamond/cBN interface shows a sharp and coherent interface structure. (b) The calculated phonon dispersions for the bulk diamond (green) and cBN (orange). (c, d) The measured phonon dispersion diagrams along the Γ–K–X–K–Γ line with the beam in the (c) diamond and (d) cBN are consistent with the calculated results. (e–g) The energy-filtered image at the specific momentum range marked by the purple rectangle in Fig. 6b. The 80–100 meV range without momentum resolution is selected for real space imaging (e), presenting uniform intensity distribution. However, the intensity maps by choosing the specific momentum areas marked by the (f) red and (g) blue rectangles show matter sensitivity. In all the color maps of intensity (counts), the lower color limit is fixed to zero, and the contrast has been adjusted for better visibility.

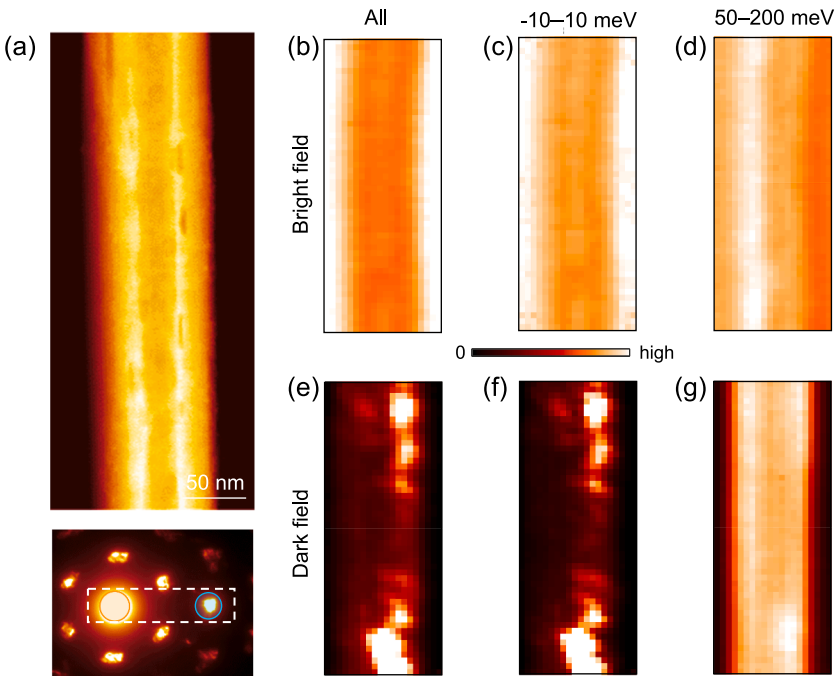

Fig. 7. Real space mapping of various components in bright and dark-field imaging. (a) A HAADF image of a BNNT tube. The bottom panel shows the electron diffraction pattern recorded at the center of the tube in the diffraction plane. The dashed rectangle represents the position of the virtual slot aperture. The orange and blue circles represent the selected momentum range for bright and dark-field imaging, respectively. (b–d) The intensity maps of different energy range with the entire EELS spectrum (b), the zero-loss peak (ZLP) corresponding to the quasi-elastic scattering (c), and the 50–200 meV primarily dominated by the phonon polariton (d) in bright field imaging. The quasi-elastic scattering includes elastic and inelastic scattering with a tiny energy transfer that cannot be distinguished due to the limited energy resolution. (e–g) The intensity maps of different energy range with the entire EELS spectrum (e), the ZLP corresponding to the quasi-elastic scattering (f), and the 50–200 meV primarily dominated by the phonons and possible phonon polaritons due to the dynamic scattering effect (g) in dark-field imaging, where the contrast is highly sensitive to defecting scattering.

dark field images respectively, where the map from the secondary diffraction spot is highly influenced by the defect scattering and show some strong hot spots appearing at the tube edge.

The entire EELS spectrum contains the elastic and inelastic scatterings with the sample. We then extract the intensity distribution at different momentum transfers of quasi-elastic scattering signals (energy of −10 meV to 10 meV, containing elastically scattered electrons and part of low-energy acoustic phonons) and phonon modes (energy of 50–200 meV) (Fig. 7c, d and f, g). Understandably, the intensity maps obtained in the −10 meV to 10 meV range show the nearly same features as that extracted from the whole EELS spectrum. Furthermore, based on the scattering theory, dipole scattering affects the interaction between the electron beam and the BNNTs at zero-momentum transfer. Hence, the phonon polariton signal will significantly affect the intensity maps extracted from the central diffraction spot. Due to its long-range Coulomb interaction, the resulting intensity maps (Fig. 7c and d) are not sensitive to structural defects. However, the slight difference in the tube wall, such as nonuniform chirality, faceting, crystal orientation, or change in the stacking order, could contribute to the intensity contrast of the EELS extracted from the central diffraction spot [64], resulting in the asymmetric intensity profiles of the left and right tube edges in Fig. 7d. As mentioned above, a larger variety of phonon modes can be activated when we select the scattered electrons with higher momentum transfers. The ZLP is much weaker and the phonon signals are explicitly visible and easier to extract. Interestingly, the intensity maps of EELS signal in 50–200 meV range extracted from the secondary diffraction spot (Fig. 7g) shows different distribution in real space, compared with that in −10 meV to −10 meV range (Fig. 7f). The contrast difference in different energy loss may derive from different kinds of defects, indicating that the stack of energy-filtered EELS maps at different momentum transfers may be a useful label to separate different defect types. Therefore, the 4D-EELS technique can be supplementary to traditional diffraction contrast imaging to decouple the scattering contributions and an effective tool to visualize and distinguish different defects, helping to study the defect-related interactions.

3.2. *More underlying physical processes extracted from 4D-EELS*

The above sections provide different operating modes in 4D-EELS based on one momentum range. Typically, as denoted in Fig. 8a, the 4D-EELS technique can simultaneously record two arbitrary areas in the diffraction plane with different momentum transfers. Therefore, we can conduct various combinations or mathematical operations among the signals in these two areas. For example, previous studies presented a differential phonon momentum map by subtracting the phonon signal at opposite reciprocal locations [88]. The intensity in such a map indicates the difference in phonon populations and can identify the direction of phonon propagation, classifying the diffuse and specular reflections in the abrupt and gradual interfaces.

Another promising application is conducting the EMCD measurement, a method based on STEM-EELS to characterize the local magnetic structure of the nanostructures, which is critical for understanding and designing the magnetism, multiferroics, and spintronics on a nanometer scale [108,109]. The basic experimental concept is to obtain two EELS spectra at opposite chiral positions of positive (marked by + in Fig. 8) and negative (marked by − in Fig. 8) in the diffraction plane. The difference between these two EELS spectra is the corresponding EMCD signals. Due to the strong dynamical diffraction effects of fast electrons, the strength and sign of the EMCD signal highly depend on the momentum transfer vectors. Typically, the circular aperture sequentially acquires the two EELS spectra twice, only collecting a small fraction of the inelastically scattered electrons, and could cause inconsistency in acquisition conditions. Compared with the conventional implementation of EMCD measurements, the 4D-EELS technique can realize a parallel acquisition of EELS spectra. This setup ensures recorded positive and negative spectra under the same acquiring conditions and negates the need for scanning the same sample area multiple times. Acquiring a complete momentum space also benefits the accurate extraction of EMCD signals.

Using the slot aperture, we measured reliable EMCD signals with a decent SNR in the yttrium iron garnet (YIG; $Y_3Fe_5O_{12}$) magnetic crystal. Fig. 8b shows the configuration of the slot aperture in the diffraction plane. As proposed by the dynamical diffraction calculation results [110], when the slot aperture places from the Left to Right position of the momentum space shown in Fig. 8b, the EMCD signal is flipped. In the experiment, the acquisition time of a single 4D-EELS dataset is approximately 8 s to ensure enough SNR. The resulting 2D intensity map versus energy and momentum transfer, which align along the energy

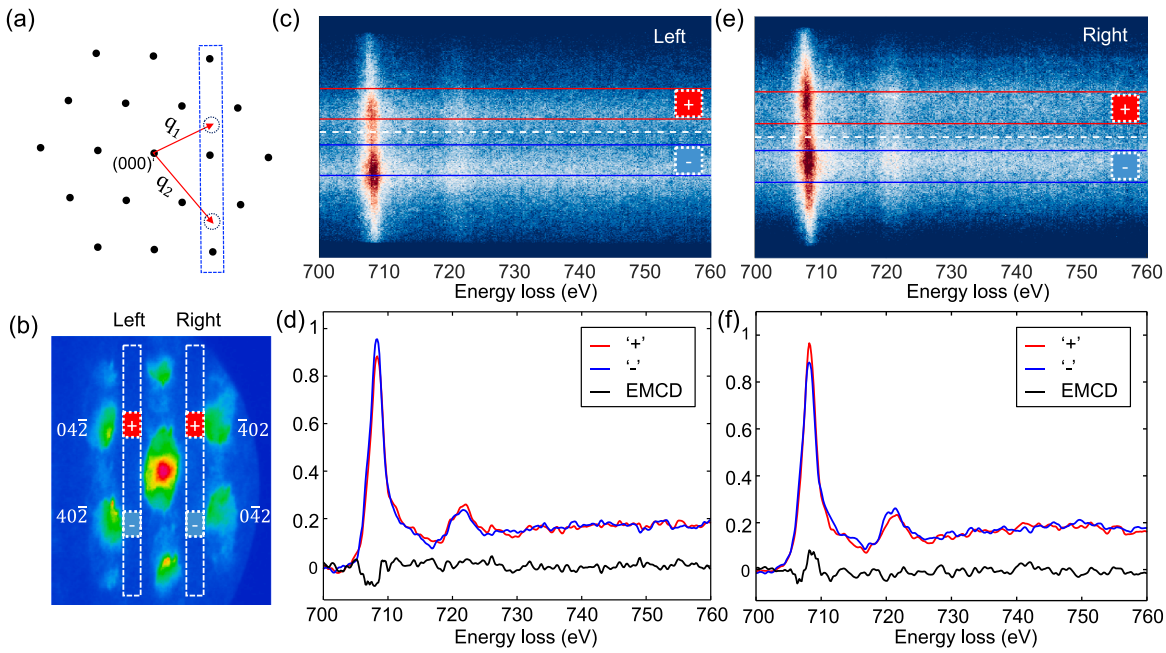

Fig. 8. Combination of two momentum transfer information from 4D-EELS. (a) A scheme of the diffraction pattern and the slot aperture configuration. The dashed circles denote the two target momentum positions. Various mathematical combinations of the EELS spectra extracted from the two positions can be performed. (b) The experimental diffraction patterns for the slot aperture (dashed rectangle) are placed on the Left and the Right sides. (c, d) Experimentally recorded *E*–**q** maps (c) and corresponding EMCD spectra (d) by extracting the chiral EELS spectra from the red and blue boxes, respectively, in the Left region. (e, f) Experimentally recorded *E*–**q** maps (e) and corresponding EMCD spectra (f) by extracting the chiral EELS spectra from the red and blue boxes, respectively, in the Right region.

axis, is correspondingly shown in Fig. 8c and e. The iron edges are visible as vertical streaks at 709 (L_3) and 723 eV (L_2). By fitting the background with the power law model in the pre-edge region, we extract the chiral EELS spectra at the Left and Right regions, normalized by integrating the intensity in a window between 740 eV and 800 eV. The blue and red spectra in Fig. 8d and f, respectively, correspond to the chiral EELS spectra at the + and − range. The sign of the obtained EMCD signal on the right side is opposite from that on the left, signifying data reliability. This measurement enables the spatially resolved EMCD to be practical, allowing us to study the effects of the surface, interface, and defects on the local magnetic properties. Furthermore, more plentiful measurements about electronic structures, such as the orbital arrangement and interband transition [111–113], should be achieved in 4D-EELS.

4. Conclusions

This study provides the physical connotation of recently developed 4D-EELS measurements and demonstrates a few applications. The unmatched spatial resolutions of STEM with an aberration corrector and the high degree of flexibility in energy and momentum dimensions adjusted by electromagnetic lenses and multipoles make it possible to closely correlate the spatial, energy, and momentum information in materials. Although the resolution of spatial and momentum cannot achieve the best because of the intrinsic tradeoff between them simultaneously, the phonon dispersion in nanoscale can be effectively mapped by scanning the electron probe and placing a slot aperture to select a specific momentum direction in the diffraction plane. In addition to the balance of spatial, momentum, and energy resolutions in the practical experiments, the tradeoff between the resolution and the SNR must be considered. From the measurable 4D dataset, we can flexibly extract real space mapping of different scattering processes, including phonon modes at various momentum transfers, which is adapted to distinguish the local inhomogeneity, such as structural, phase, and element variations. Furthermore, the collection of spectra contributions at different momentum range in the acquired 4D dataset allows for obtaining reliable EMCD signals and much more dynamic processes. These results exhibit the perspective of the 4D-EELS technique in probing nanoscale thermal, mechanical, optical, and electronic properties.

However, it should be appreciated some limitations and space still exist for development in the 4D-EELS technique. First, although sub-10 meV energy resolutions are feasible because it works well for those light element systems with high-energy phonons, for most materials with heavy atoms, their data quality and extractable knowledge of phonon dispersion are limited by the energy resolution. Besides, even though compared with the measurement with large convergence semi-angles, which averages all the signals over the entire BZs, the momentum-resolved 4D-EELS data allow us to remove the background of the spectra more accurately but is still restricted by the attainable energy resolution in STEM-EELS. For example, the details in acoustic phonon modes, specifically at the small q, are challenging to extract. Therefore, better energy resolution is highly desirable. Moreover, given the complexity of the scattering between the electron beam and the sample, precise and efficient data processing and sophisticated theoretical simulation are required to interpret the obtained signal and reveal the deep physical properties. In addition to providing a direct picture of the spatial, energy, and momentum dimensions, a further combination of multiple dimensions, such as time and temperature, by local external field modulation will promote the abundant development of the 4D-EELS technique and broaden the applications of this technique.

Declaration of Competing Interest

The authors declare that they have no known competing financial interests or personal relationships that could have appeared to influence the work reported in this paper.

Data availability

Data will be made available on request.

Acknowledgments

The work was supported by the National Natural Science Foundation of China (52125307, 11974023, 52021006), the "2011 Program" from the Peking-Tsinghua-IOP Collaborative Innovation Center of Quantum Matter, Youth Innovation Promotion Association, CAS. We acknowledge Electron Microscopy Laboratory of Peking University for the use of electron microscopes. We acknowledge High-performance Computing Platform of Peking University for providing computational resources for the DFPT calculation. P.G. acknowledges support from the Tencent Foundation through the XPLORER PRIZE.

Reference

[1] A. Kumar, P.K. Ahluwalia, Electronic structure of transition metal dichalcogenides monolayers 1H-MX2 (M = Mo, W; X = S, Se, Te) from ab-initio theory: new direct band gap semiconductors, Eur. Phys. J. B 85 (2012) 186.
[2] M. Zacharias, C.E. Patrick, F. Giustino, Stochastic approach to phonon-assisted optical absorption, Phys. Rev. Lett. 115 (2015) 177401.
[3] E.M. Hutter, M.C. Gélvez-Rueda, A. Osherov, V. Bulović, F.C. Grozema, S. D. Stranks, T.J. Savenije, Direct–indirect character of the bandgap in methylammonium lead iodide perovskite, Nat. Mater. 16 (2017) 115–120.
[4] J. Noffsinger, E. Kioupakis, C.G. Van De Walle, S.G. Louie, M.L. Cohen, Phonon-assisted optical absorption in silicon from first principles, Phys. Rev. Lett. 108 (2012) 167402.
[5] G. Onida, L. Reining, A. Rubio, Electronic excitations: density-functional versus many-body Green's-function approaches, Rev. Mod. Phys. 74 (2002) 601–659.
[6] C.W. Li, J. Hong, A.F. May, D. Bansal, S. Chi, T. Hong, G. Ehlers, O. Delaire, Orbitally driven giant phonon anharmonicity in SnSe, Nat. Phys. 11 (2015) 1063–1069.
[7] A. Kanigel, U. Chatterjee, M. Randeria, M.R. Norman, G. Koren, K. Kadowaki, J. C. Campuzano, Evidence for pairing above the transition temperature of cuprate superconductors from the electronic dispersion in the pseudogap phase, Phys. Rev. Lett. 101 (2008) 137002.
[8] G. Xu, B. Lian, P. Tang, X.-L. Qi, S.-C. Zhang, Topological superconductivity on the surface of Fe-based superconductors, Phys. Rev. Lett. 117 (2016), 047001.
[9] D.J. Scalapino, S.R. White, S. Zhang, Insulator, metal, or superconductor: the criteria, Phys. Rev. B 47 (1993) 7995–8007.
[10] Y. Cao, V. Fatemi, S. Fang, K. Watanabe, T. Taniguchi, E. Kaxiras, P. Jarillo-Herrero, Unconventional superconductivity in magic-angle graphene superlattices, Nature 556 (2018) 43–50.
[11] K.U.N. Huang, Lattice vibrations and optical waves in ionic crystals, Nature 167 (1951) 779–780.
[12] P.B. Allen, Electron-phonon effects in the infrared properties of metals, Phys. Rev. B 3 (1971) 305–320.
[13] T. Dekorsy, H. Auer, H.J. Bakker, H.G. Roskos, H. Kurz, THz electromagnetic emission by coherent infrared-active phonons, Phys. Rev. B 53 (1996) 4005–4014.
[14] T. Dekorsy, V.A. Yakovlev, W. Seidel, M. Helm, F. Keilmann, Infrared-phonon-polariton resonance of the nonlinear susceptibility in GaAs, Phys. Rev. Lett. 90 (2003), 055508.
[15] K. Huang, M. Born, On the interaction between the radiation field and ionic crystals, Proc. R. Soc. Lond. A Math. Phys. Sci. 208 (1951) 352–365.
[16] Z. Zheng, J. Chen, Y. Wang, X. Wang, X. Chen, P. Liu, J. Xu, W. Xie, H. Chen, S. Deng, N. Xu, Highly confined and tunable hyperbolic phonon polaritons in van der waals semiconducting transition metal oxides, Adv. Mater. 30 (2018), 1705318.
[17] P.-A. Mante, Y.-R. Huang, S.-C. Yang, T.-M. Liu, A.A. Maznev, J.-K. Sheu, C.-K. Sun, THz acoustic phonon spectroscopy and nanoscopy by using piezoelectric semiconductor heterostructures, Ultrasonics 56 (2015) 52–65.
[18] A. Debernardi, S. Baroni, E. Molinari, Anharmonic phonon lifetimes in semiconductors from density-functional perturbation theory, Phys. Rev. Lett. 75 (1995) 1819–1822.
[19] O. Delaire, J. Ma, K. Marty, A.F. May, M.A. McGuire, M.H. Du, D.J. Singh, A. Podlesnyak, G. Ehlers, M.D. Lumsden, B.C. Sales, Giant anharmonic phonon scattering in PbTe, Nat. Mater. 10 (2011) 614–619.
[20] W. Li, J. Carrete, N.A. Katcho, N. Mingo, ShengBTE: a solver of the Boltzmann transport equation for phonons, Comput. Phys. Commun. 185 (2014) 1747–1758.
[21] X. Qian, J. Zhou, G. Chen, Phonon-engineered extreme thermal conductivity materials, Nat. Mater. 20 (2021) 1188–1202.
[22] D.G. Cahill, W.K. Ford, K.E. Goodson, G.D. Mahan, A. Majumdar, H.J. Maris, R. Merlin, S.R. Phillpot, Nanoscale thermal transport, J. Appl. Phys. 93 (2003) 793–818.
[23] N. Mingo, Calculation of Si nanowire thermal conductivity using complete phonon dispersion relations, Phys. Rev. B 68 (2003) 113308.
[24] R. Qi, R. Shi, Y. Li, Y. Sun, M. Wu, N. Li, J. Du, K. Liu, C. Chen, J. Chen, F. Wang, D. Yu, E.G. Wang, P. Gao, Measuring phonon dispersion at an interface, Nature 599 (2021) 399–403.
[25] A. Gozar, G. Logvenov, L.F. Kourkoutis, A.T. Bollinger, L.A. Giannuzzi, D. A. Muller, I. Bozovic, High-temperature interface superconductivity between metallic and insulating copper oxides, Nature 455 (2008) 782–785.
[26] J.A. Mundy, C.M. Brooks, M.E. Holtz, J.A. Moyer, H. Das, A.F. Rebola, J.T. Heron, J.D. Clarkson, S.M. Disseler, Z. Liu, A. Farhan, R. Held, R. Hovden, E. Padgett, Q. Mao, H. Paik, R. Misra, L.F. Kourkoutis, E. Arenholz, A. Scholl, J.A. Borchers, W.D. Ratcliff, R. Ramesh, C.J. Fennie, P. Schiffer, D.A. Muller, D.G. Schlom, Atomically engineered ferroic layers yield a room-temperature magnetoelectric multiferroic, Nature 537 (2016) 523–527.
[27] M.J. Lagos, A. Trugler, U. Hohenester, P.E. Batson, Mapping vibrational surface and bulk modes in a single nanocube, Nature 543 (2017) 529–532.
[28] G. Hodes, When small is different: some recent advances in concepts and applications of nanoscale phenomena, Adv. Mater. 19 (2007), 1307-1307.
[29] I. Khan, K. Saeed, I. Khan, Nanoparticles: properties, applications and toxicities, Arab. J. Chem. 12 (2019) 908–931.
[30] N. Baig, I. Kammakakam, W. Falath, Nanomaterials: a review of synthesis methods, properties, recent progress, and challenges, Mater. Adv. 2 (2021) 1821–1871.
[31] J. Jeevanandam, A. Barhoum, Y.S. Chan, A. Dufresne, M.K. Danquah, Review on nanoparticles and nanostructured materials: history, sources, toxicity and regulations, Beilstein J. Nanotechnol. 9 (2018) 1050–1074.
[32] H.Y. Hwang, Y. Iwasa, M. Kawasaki, B. Keimer, N. Nagaosa, Y. Tokura, Emergent phenomena at oxide interfaces, Nat. Mater. 11 (2012) 103–113.
[33] M.M. Waldrop, The chips are down for Moore's law, Nature 530 (2016) 144–147.
[34] Y. Pei, N.A. Heinz, A. Lalonde, G.J. Snyder, Combination of large nanostructures and complex band structure for high performance thermoelectric lead telluride, Energy Environ. Sci. 4 (2011) 3640.
[35] M.F. Hochella Jr., D.W. Mogk, J. Ranville, I.C. Allen, G.W. Luther, L.C. Marr, B. P. McGrail, M. Murayama, N.P. Qafoku, K.M. Rosso, N. Sahai, P.A. Schroeder, P. Vikesland, P. Westerhoff, Y. Yang, Natural, incidental, and engineered nanomaterials and their impacts on the Earth system, Science 363 (2019) eaau8299.
[36] S. Mitragotri, D.G. Anderson, X. Chen, E.K. Chow, D. Ho, A.V. Kabanov, J. M. Karp, K. Kataoka, C.A. Mirkin, S.H. Petrosko, J. Shi, M.M. Stevens, S. Sun, S. Teoh, S.S. Venkatraman, Y. Xia, S. Wang, Z. Gu, C. Xu, Accelerating the translation of nanomaterials in biomedicine, ACS Nano 9 (2015) 6644–6654.
[37] J. Lee, K.T. Crampton, N. Tallarida, V.A. Apkarian, Visualizing vibrational normal modes of a single molecule with atomically confined light, Nature 568 (2019) 78–82.
[38] X. Yan, C. Liu, C.A. Gadre, L. Gu, T. Aoki, T.C. Lovejoy, N. Dellby, O.L. Krivanek, D.G. Schlom, R. Wu, X. Pan, Single-defect phonons imaged by electron microscopy, Nature 589 (2021) 65–69.
[39] J. Kalt, M. Sternik, I. Sergueev, J. Herfort, B. Jenichen, H.C. Wille, O. Sikora, P. Piekarz, K. Parlinski, T. Baumbach, S. Stankov, Lattice dynamics of epitaxial strain-free interfaces, Phys. Rev. B 98 (2018) 121409.
[40] A. Seiler, P. Piekarz, S. Ibrahimkutty, D.G. Merkel, O. Waller, R. Pradip, A. I. Chumakov, R. Rüffer, T. Baumbach, K. Parlinski, M. Fiederle, S. Stankov, Anomalous lattice dynamics of $EuSi_2$ nanoislands: role of interfaces unveiled, Phys. Rev. Lett. 117 (2016) 276101.
[41] R. Venkatasubramanian, E. Siivola, T. Colpitts, B. O'Quinn, Thin-film thermoelectric devices with high room-temperature figures of merit, Nature 413 (2001) 597–602.
[42] A.J. Minnich, M.S. Dresselhaus, Z.F. Ren, G. Chen, Bulk nanostructured thermoelectric materials: current research and future prospects, Energy Environ. Sci. 2 (2009) 466–479.
[43] B. Poudel, Q. Hao, Y. Ma, Y. Lan, A. Minnich, B. Yu, X. Yan, D. Wang, A. Muto, D. Vashaee, X. Chen, J. Liu, M.S. Dresselhaus, G. Chen, Z. Ren, High-thermoelectric performance of nanostructured bismuth antimony telluride bulk alloys, Science 320 (2008) 634–638.
[44] M. Li, Z. Ding, Q. Meng, J. Zhou, Y. Zhu, H. Liu, M.S. Dresselhaus, G. Chen, Nonperturbative quantum nature of the dislocation–phonon interaction, Nano Lett. 17 (2017) 1587–1594.
[45] C. Tang, C. Liu, G. Zhou, F. Li, H. Ding, Z. Li, D. Zhang, Z. Li, C. Song, S. Ji, K. He, L. Wang, X. Ma, Q.-K. Xue, Interface-enhanced electron-phonon coupling and high-temperature superconductivity in potassium-coated ultrathin FeSe films on $SrTiO_3$, Phys. Rev. B 93 (2016), 020507.
[46] M.J. Lagos, A. Trügler, U. Hohenester, P.E. Batson, Mapping vibrational surface and bulk modes in a single nanocube, Nature 543 (2017) 529–532.
[47] A.A. Govyadinov, A. Konečná, A. Chuvilin, S. Vélez, I. Dolado, A.Y. Nikitin, S. Lopatin, F. Casanova, L.E. Hueso, J. Aizpurua, R. Hillenbrand, Probing low-energy hyperbolic polaritons in van der Waals crystals with an electron microscope, Nat. Commun. 8 (2017) 95.
[48] X. Li, G. Haberfehlner, U. Hohenester, O. Stéphan, G. Kothleitner, M. Kociak, Three-dimensional vectorial imaging of surface phonon polaritons, Science 371 (2021) 1364–1367.
[49] N. Choudhury, S.L. Chaplot, Inelastic neutron scattering and lattice dynamics of minerals, Pramana 71 (2008) 819–828.
[50] A. Lewis, H. Taha, A. Strinkovski, A. Manevitch, A. Khatchatouriants, R. Dekhter, E. Ammann, Near-field optics: from subwavelength illumination to nanometric shadowing, Nat. Biotechnol. 21 (2003) 1378–1386.
[51] J. Olson, S. Dominguez-Medina, A. Hoggard, L.Y. Wang, W.S. Chang, S. Link, Optical characterization of single plasmonic nanoparticles, Chem. Soc. Rev. 44 (2015) 40–57.
[52] P. Verma, Tip-enhanced raman spectroscopy: technique and recent advances, Chem. Rev. 117 (2017) 6447–6466.
[53] R.C. Dunn, Near-field scanning optical microscopy, Chem. Rev. 99 (1999) 2891–2928.
[54] H. Ibach, D.L. Mills, Electron Energy Loss Spectroscopy and Surface Vibrations, Academic Press, New York, 1982.

[55] C. Colliex, From early to present and future achievements of EELS in the TEM, Eur. Phys. J. Spec. Top. 97 (2022) 38.
[56] X. Yan, C.A. Gadre, T. Aoki, X. Pan, Probing molecular vibrations by monochromated electron microscopy, Trends Chem. 4 (2022) 76–90.
[57] O.L. Krivanek, T.C. Lovejoy, N. Dellby, T. Aoki, R.W. Carpenter, P. Rez, E. Soignard, J. Zhu, P.E. Batson, M.J. Lagos, R.F. Egerton, P.A. Crozier, Vibrational spectroscopy in the electron microscope, Nature 514 (2014) 209–212.
[58] R. Senga, K. Suenaga, P. Barone, S. Morishita, F. Mauri, T. Pichler, Position and momentum mapping of vibrations in graphene nanostructures, Nature 573 (2019) 247–250.
[59] O.L. Krivanek, N. Dellby, J.A. Hachtel, J.-C. Idrobo, M. Hotz, B. Plotkin-Swing, N. J. Bacon, A.L. Bleloch, G.J. Corbin, M.V. Hoffman, Progress in ultrahigh energy resolution EELS, Ultramicroscopy 203 (2019) 60–67.
[60] T.C. Lovejoy, N.J. Bacon, A.L. Bleloch, N. Dellby, M.V. Hoffman, O.L. Krivanek, Ultra-high energy resolution EELS, Microsc. Microanal. 23 (2017) 1552–1553.
[61] F. Hage, Q. Ramasse, L. Allen, Contrast reversal in atomic-scale phonon spectroscopic imaging, Phys. Rev. B 102 (2020), 214111.
[62] J.R. Jokisaari, J.A. Hachtel, X. Hu, A. Mukherjee, C. Wang, A. Konecna, T. C. Lovejoy, N. Dellby, J. Aizpurua, O.L. Krivanek, J.-C. Idrobo, R.F. Klie, Vibrational spectroscopy of water with high spatial resolution, Adv. Mater. 30 (2018), 1802702.
[63] S.M. Collins, D.M. Kepaptsoglou, J. Hou, C.W. Ashling, G. Radtke, T.D. Bennett, P. A. Midgley, Q.M. Ramasse, Functional group mapping by electron beam vibrational spectroscopy from nanoscale volumes, Nano Lett. 20 (2020) 1272–1279.
[64] K. Venkatraman, B.D.A. Levin, K. March, P. Rez, P.A. Crozier, Vibrational spectroscopy at atomic resolution with electron impact scattering, Nat. Phys. 15 (2019) 1237–1241.
[65] F.S. Hage, G. Radtke, D.M. Kepaptsoglou, M. Lazzeri, Q.M. Ramasse, Single-atom vibrational spectroscopy in the scanning transmission electron microscope, Science 367 (2020) 1124–1127.
[66] O.L. Krivanek, T.C. Lovejoy, M.F. Murfitt, G. Skone, P.E. Batson, N. Dellby, Towards sub-10 meV energy resolution STEM-EELS, J. Phys. Conf. Ser. 522 (2014), 012023.
[67] F.S. Hage, R.J. Nicholls, J.R. Yates, D.G. McCulloch, T.C. Lovejoy, N. Dellby, O. L. Krivanek, K. Refson, Q.M. Ramasse, Nanoscale momentum-resolved vibrational spectroscopy, Sci. Adv. 4 (2018) eaar7495.
[68] J.A. Hachtel, J. Huang, I. Popovs, S. Jansone-Popova, J.K. Keum, J. Jakowski, T. C. Lovejoy, N. Dellby, O.L. Krivanek, J.C. Idrobo, Identification of site-specific isotopic labels by vibrational spectroscopy in the electron microscope, Science 363 (2019) 525–528.
[69] K. Kimoto, G. Kothleitner, W. Grogger, Y. Matsui, F. Hofer, Advantages of a monochromator for bandgap measurements using electron energy-loss spectroscopy, Micron 36 (2005) 185–189.
[70] T. Miyata, M. Fukuyama, A. Hibara, E. Okunishi, M. Mukai, T. Mizoguchi, Measurement of vibrational spectrum of liquid using monochromated scanning transmission electron microscopy–electron energy loss spectroscopy, Microscopy 63 (2014) 377–382.
[71] S. Lopatin, B. Cheng, W.T. Liu, M.L. Tsai, J.H. He, A. Chuvilin, Optimization of monochromated TEM for ultimate resolution imaging and ultrahigh resolution electron energy loss spectroscopy, Ultramicroscopy 184 (2018) 109–115.
[72] N. Dellby, T. Lovejoy, G. Corbin, N. Johnson, R. Hayner, M. Hoffman, P. Hrncrik, B. Plotkin-Swing, D. Taylor, O. Krivanek, Ultra-high energy resolution EELS, Microsc. Microanal. 26 (2020) 1804–1805.
[73] R. Qi, N. Li, J. Du, R. Shi, Y. Huang, X. Yang, L. Liu, Z. Xu, Q. Dai, D. Yu, P. Gao, Four-dimensional vibrational spectroscopy for nanoscale mapping of phonon dispersion in BN nanotubes, Nat. Commun. 12 (2021) 1179.
[74] S. Huang, R. Shi, Y. Li, M. Wu, N. Li, J. Du, D. Yu, P. Gao, Recent progress of vibrational electron energy-loss spectroscopy in scanning transmission electron microscope, Zhenkong Kexue Yu Jishu Xuebao 41 (2021) 213–224.
[75] Y. Li, R. Qi, R. Shi, N. Li, P. Gao, Manipulation of surface phonon polaritons in SiC nanorods, Sci. Bull. 65 (2020) 820–826.
[76] R. Egerton, Electron Energy-Loss Spectroscopy in the Electron Microscope, 3rd Edition, Springer, 2011, p. 2011.
[77] P.B. Hirsch, A. Howie, M.J. Whelan, A kinematical theory of diffraction contrast of electron transmission microscope images of dislocations and other defects, Philos. Trans. A Math. Phys. Eng. Sci. 252 (1960) 499–529.
[78] D.J.H. Cockayne, I.L.F. Ray, M.J. Whelan, Investigations of dislocation strain fields using weak beams, Philos. Mag. 20 (1969) 1265–1270.
[79] C. Ophus, Four-dimensional scanning transmission electron microscopy (4D-STEM): from scanning nanodiffraction to ptychography and beyond, Microsc. Microanal. 25 (2019) 563–582.
[80] M.W. Tate, P. Purohit, D. Chamberlain, K.X. Nguyen, R. Hovden, C.S. Chang, P. Deb, E. Turgut, J.T. Heron, D.G. Schlom, D.C. Ralph, G.D. Fuchs, K.S. Shanks, H.T. Philipp, D.A. Muller, S.M. Gruner, High dynamic range pixel array detector for scanning transmission electron microscopy, Microsc. Microanal. 22 (2016) 237–249.
[81] T. Lovejoy, B. Plotkin-Swing, N. Dellby, C. Meyer, A. Mittelberger, A. Eljarrat, B. Haas, C. Koch, O. Krivanek, Angle-resolved electron energy loss spectroscopy, Microsc. Microanal. 26 (2020) 964–965.
[82] K. Kimoto, T. Asaka, T. Nagai, M. Saito, Y. Matsui, K. Ishizuka, Element-selective imaging of atomic columns in a crystal using STEM and EELS, Nature 450 (2007) 702–704.
[83] B. Plotkin-Swing, G. Corbin, N. Dellby, N. Johnson, P. Hrncrik, C. Meyer, A. Mittelberger, D. Taylor, O. Krivanek, T. Lovejoy, Advances in momentum resolved EELS, Microsc. Microanal. 27 (2021) 136–138.
[84] P.E. Batson, N. Dellby, O.L. Krivanek, Sub-ångstrom resolution using aberration corrected electron optics, Nature 418 (2002) 617–620.
[85] T. Lovejoy, G. Corbin, N. Dellby, M. Hoffman, O. Krivanek, Advances in ultra-high energy resolution STEM-EELS, Microsc. Microanal. 24 (2018) 446–447.
[86] J. Hong, R. Senga, T. Pichler, K. Suenaga, Probing exciton dispersions of freestanding monolayer WSe_2 by momentum, Phys. Rev. Lett. 124 (2020), 087401.
[87] B. Liu, Y.-T. Zhang, R. Qiao, R. Shi, Y. Li, Q. Guo, J. Li, X. Li, L. Wang, J. Qi, Tunable interband transitions in twisted h-BN/graphene heterostructures, Phys. Rev. Lett. 131 (2023), 016201.
[88] C.A. Gadre, X. Yan, Q. Song, J. Li, L. Gu, H. Huyan, T. Aoki, S.-W. Lee, G. Chen, R. Wu, X. Pan, Nanoscale imaging of phonon dynamics by electron microscopy, Nature 606 (2022) 292–297.
[89] Y.H. Li, R.S. Qi, R.C. Shi, J.N. Hu, Z.T. Liu, Y.W. Sun, M.Q. Li, N. Li, C.L. Song, L. Wang, Z.B. Hao, Y. Luo, Q.K. Xue, X.C. Ma, P. Gao, Atomic-scale probing of heterointerface phonon bridges in nitride semiconductor, Proc. Natl. Acad. Sci. U. S.A. 119 (2022), e2117027119.
[90] E.R. Hoglund, D.L. Bao, A. O'Hara, S. Makarem, Z.T. Piontkowski, J.R. Matson, A. K. Yadav, R.C. Haislmaier, R. Engel-Herbert, J.F. Ihlefeld, J. Ravichandran, R. Ramesh, J.D. Caldwell, T.E. Beechem, J.A. Tomko, J.A. Hachtel, S. T. Pantelides, P.E. Hopkins, J.M. Howe, Emergent interface vibrational structure of oxide superlattices, Nature 601 (2022) 556–561.
[91] B. Plotkin-Swing, G.J. Corbin, S. De Carlo, N. Dellby, C. Hoermann, M. V. Hoffman, T.C. Lovejoy, C.E. Meyer, A. Mittelberger, R. Pantelic, L. Piazza, O. L. Krivanek, Hybrid pixel direct detector for electron energy loss spectroscopy, Ultramicroscopy 217 (2020), 113067.
[92] D.B. Williams, C.B. Carter, Transmission Electron Microscopy: a Textbook for Materials Science Vol. 2, Springer Science & Business Media, 2009, pp. 23–38.
[93] N. Dellby, O.L. Krivanek, N.J. Bacon, G.J. Corbin, N. Johnson, R. Hayner, P. Hrncrik, B. Plotkin-Swing, D. Taylor, Z.S. Szilaygi, T.C. Lovejoy, E.E.L.S. Multi-Sun, Ultra-high energy resolution combined with high spatial resolution and high beam current, Microsc. Microanal. 28 (2022) 2640–2642.
[94] P.E. Batson, M.J. Lagos, Interpretation of meV resolution phonon EELS data, Microsc. Microanal. 24 (2018) 412–413.
[95] R.H. Ritchie, A. Howie, Inelastic scattering probabilities in scanning transmission electron microscopy, Philos. Mag. A 58 (1988) 753–767.
[96] R.J. Nicholls, F.S. Hage, D.G. McCulloch, Q.M. Ramasse, K. Refson, J.R. Yates, Theory of momentum-resolved phonon spectroscopy in the electron microscope, Phys. Rev. B 99 (2019), 094105.
[97] L.J. Allen, H.G. Brown, S.D. Findlay, B.D. Forbes, A quantum mechanical exploration of phonon energy-loss spectroscopy using electrons in the aloof beam geometry, Microscopy (Oxf) 67 (2018) i24–i29.
[98] F. Roth, A. König, J. Fink, B. Büchner, M. Knupfer, Electron energy-loss spectroscopy: a versatile tool for the investigations of plasmonic excitations, J. Electron Spectrosc. Relat. Phenom. 195 (2014) 85–95.
[99] D. Waasmaier, A. Kirfel, New analytical scattering-factor functions for free atoms and ions, Acta Crystallogr. 51 (1995) 416–431.
[100] C. Dwyer, T. Aoki, P. Rez, S.L. Chang, T.C. Lovejoy, O.L. Krivanek, Electron-beam mapping of vibrational modes with nanometer spatial resolution, Phys. Rev. Lett. 117 (2016), 256101.
[101] C. Dwyer, Localization of high-energy electron scattering from atomic vibrations, Phys. Rev. B 89 (2014), 054103.
[102] B. Forbes, L. Allen, Modeling energy-loss spectra due to phonon excitation, Phys. Rev. B 94 (2016), 014110.
[103] N. Li, X. Guo, X. Yang, R. Qi, T. Qiao, Y. Li, R. Shi, Y. Li, K. Liu, Z. Xu, L. Liu, F. J. Garcia de Abajo, Q. Dai, E.G. Wang, P. Gao, Direct observation of highly confined phonon polaritons in suspended monolayer hexagonal boron nitride, Nat. Mater. 20 (2021) 43–48.
[104] A.A. Govyadinov, A. Konečná, A. Chuvilin, S. Vélez, I. Dolado, A.Y. Nikitin, S. Lopatin, F. Casanova, L.E. Hueso, J. Aizpurua, Probing low-energy hyperbolic polaritons in van der Waals crystals with an electron microscope, Nat. Commun. 8 (2017) 1–10.
[105] W. Grogger, M. Varela, R. Ristau, B. Schaffer, F. Hofer, K.M. Krishnan, Energy-filtering transmission electron microscopy on the nanometer length scale, J. Electron Spectrosc. Relat. Phenom. 143 (2005) 139–147.
[106] P.J. Thomas, P.A. Midgley, An introduction to energy-filtered transmission electron microscopy, Top. Catal. 21 (2002) 109–138.
[107] J.A. Hunt, D.B. Williams, Electron energy-loss spectrum-imaging, Ultramicroscopy 38 (1991) 47–73.
[108] C. Hébert, P. Schattschneider, A proposal for dichroic experiments in the electron microscope, Ultramicroscopy 96 (2003) 463–468.
[109] P. Schattschneider, S. Rubino, C. Hébert, J. Rusz, J. Kuneš, P. Novák, E. Carlino, M. Fabrizioli, G. Panaccione, G. Rossi, Detection of magnetic circular dichroism using a transmission electron microscope, Nature 441 (2006) 486–488.
[110] D. Song, J. Rusz, J. Cai, J. Zhu, Detection of electron magnetic circular dichroism signals under zone axial diffraction geometry, Ultramicroscopy 169 (2016) 44–54.

[111] A. Gloter, M.W. Chu, M. Kociak, C.H. Chen, C. Colliex, Probing non-dipole allowed excitations in highly correlated materials with nanoscale resolution, Ultramicroscopy 109 (2009) 1333–1337.
[112] M. Bugnet, M. Ederer, V.K. Lazarov, L. Li, Q.M. Ramasse, S. Loffler, D. M. Kepaptsoglou, Imaging the spatial distribution of electronic states in graphene using electron energy-loss spectroscopy: prospect of orbital mapping, Phys. Rev. Lett. 128 (2022), 116401.
[113] S. Loffler, M. Bugnet, N. Gauquelin, S. Lazar, E. Assmann, K. Held, G.A. Botton, P. Schattschneider, Real-space mapping of electronic orbitals, Ultramicroscopy 177 (2017) 26–29.